https://doi.org/10.3847/1538-4357/abafc3

CrossMark

Disentangling the Cosmic Web toward FRB 190608

Sunil Simha[1] , Joseph N. Burchett[1,2] , J. Xavier Prochaska[1,3] , Jay S. Chittidi[4] , Oskar Elek[1] , Nicolas Tejos[5] ,
Regina Jorgenson[4] , Keith W. Bannister[6] , Shivani Bhandari[6] , Cherie K. Day[6,7] , Adam T. Deller[7] , Angus G. Forbes[1] ,
Jean-Pierre Macquart[8] , Stuart D. Ryder[9,10] , and Ryan M. Shannon[7]

[1] University of California—Santa Cruz, 1156 High St., Santa Cruz, CA 95064, USA; shassans@ucsc.edu
[2] New Mexico State University, P.O. Box 30001, MSC 4500, Las Cruces, NM 88001, USA
[3] Kavli Institute for the Physics and Mathematics of the Universe, 5-1-5 Kashiwanoha, Kashiwa, 277-8583, Japan
[4] Maria Mitchell Observatory, 4 Vestal Street, Nantucket, MA 02554, USA
[5] Instituto de Física, Pontificia Universidad Católica de Valparaíso, Casilla 4059, Valparaíso, Chile
[6] Australia Telescope National Facility, CSIRO Astronomy and Space Science, P.O. Box 76, Epping, NSW 1710, Australia
[7] Centre for Astrophysics and Supercomputing, Swinburne University of Technology, Hawthorn, VIC 3122, Australia
[8] International Centre for Radio Astronomy Research, Curtin University, Bentley, WA 6102, Australia
[9] Department of Physics & Astronomy, Macquarie University, NSW 2109, Australia
[10] Macquarie University Research Centre for Astronomy, Astrophysics & Astrophotonics, Sydney, NSW 2109, Australia

Abstract

Fast radio burst (FRB) 190608 was detected by the Australian Square Kilometre Array Pathfinder (ASKAP) and localized to a spiral galaxy at $z_{host} = 0.11778$ in the Sloan Digital Sky Survey (SDSS) footprint. The burst has a large dispersion measure ($DM_{FRB} = 339.8$ pc cm^{-3}) compared to the expected cosmic average at its redshift. It also has a large rotation measure ($RM_{FRB} = 353$ rad m^{-2}) and scattering timescale ($\tau = 3.3$ ms at 1.28 GHz). Chittidi et al. perform a detailed analysis of the ultraviolet and optical emission of the host galaxy and estimate the host DM contribution to be 110 ± 37 pc cm^{-3}. This work complements theirs and reports the analysis of the optical data of galaxies in the foreground of FRB 190608 in order to explore their contributions to the FRB signal. Together, the two studies delineate an observationally driven, end-to-end study of matter distribution along an FRB sightline, the first study of its kind. Combining our Keck Cosmic Web Imager (KCWI) observations and public SDSS data, we estimate the expected cosmic dispersion measure DM_{cosmic} along the sightline to FRB 190608. We first estimate the contribution of hot, ionized gas in intervening virialized halos ($DM_{halos} \approx$ 7–28 pc cm^{-3}). Then, using the Monte Carlo Physarum Machine methodology, we produce a 3D map of ionized gas in cosmic web filaments and compute the DM contribution from matter outside halos ($DM_{IGM} \approx$ 91–126 pc cm^{-3}). This implies that a greater fraction of ionized gas along this sightline is extant outside virialized halos. We also investigate whether the intervening halos can account for the large FRB rotation measure and pulse width and conclude that it is implausible. Both the pulse broadening and the large Faraday rotation likely arise from the progenitor environment or the host galaxy.

Unified Astronomy Thesaurus concepts: Galaxy dark matter halos (1880); Quasar absorption line spectroscopy (1317); Galaxy evolution (594); Intergalactic medium (813); Radio transient sources (2008)

Supporting material: machine-readable table

1. Introduction

Galaxies are the result of gravitational accretion of baryons onto dark matter halos, i.e., the dense gas that has cooled and condensed to form dust, stars, and planets. The dark matter halos, according to simulations, are embedded in the cosmic web, a filamentary structure of matter (e.g., Springel et al. 2005). The accretion process of galaxies is further predicted, at least for halo masses $M_{halo} \gtrsim 10^{12} M_{\odot}$, to generate a halo of baryons, most likely dominated by gas shock-heated to the virial temperature of the potential well (White & Rees 1978; White & Frenk 1991; Kauffmann et al. 1993; Somerville & Primack 1999; Cole et al. 2000). At $T \gtrsim 10^6$ K and $n_e \sim 10^{-4}$ cm^{-3}, however, this halo gas is very difficult to detect in emission (Kuntz & Snowden 2000; Yoshino et al. 2009; Henley & Shelton 2013) and similarly challenging to observe in absorption (e.g., Burchett et al. 2019). And while experiments leveraging the Sunyaev–Zeldovich effect are promising (Planck Collaboration et al. 2016b), these are currently limited to massive halos and are subject to significant systematic effects (Lim et al. 2020).

Therefore, there has been a wide range of predictions for the mass fraction of baryons in massive halos, from $\approx 10\%$ to nearly the full complement relative to the cosmic mean Ω_b/Ω_m (Pillepich et al. 2018). Here, Ω_b and Ω_m are the average cosmic densities of baryons and matter respectively. Underlying this order-of-magnitude spread in predictions are uncertain physical processes that eject gas from galaxies and can greatly shape them and their environments (e.g., Suresh et al. 2015).

Fast radio bursts (FRBs) are dispersed by intervening ionized matter such that the pulse arrival delay, with respect to a reference frequency, scales as the inverse square of frequency times the dispersion measure, DM. DM is the path integral of the electron density, n_e, weighted by the scale factor $(1 + z)^{-1}$, i.e., $DM \equiv \int n_e \, ds/(1 + z)$. These FRB measurements are sensitive to all of the ionized gas along the sightline. Therefore, they have the potential to trace the otherwise invisible plasma surrounding and in between galaxy halos (Macquart et al. 2020). The Fast and Fortunate for FRB Follow-up (F^4) team[11] has initiated a program to disentangle the cosmic web by

_____

[11] http://www.ucolick.org/f-4

correlating the dispersion measure of FRBs with the distributions of foreground galaxy halos (McQuinn 2014; Prochaska & Zheng 2019). This article marks our first effort.

Since the DM is an additive quantity, it may be split into individual contributions of intervening, ionized gas reservoirs:

$$DM_{FRB} = DM_{MW} + DM_{cosmic} + DM_{host}. \qquad (1)$$

Here, DM_{MW} refers to the contribution from the Milky Way, which is further split into its contributions from the interstellar medium (ISM) and halo gas ($DM_{MW,ISM}$ and $DM_{MW,halo}$ respectively). Additionally, DM_{host} is the net contribution from the host galaxy and its halo, including any contribution from the immediate environment of the FRB progenitor. Meanwhile, DM_{cosmic} is the sum of contributions from gas in the circumgalactic medium (CGM) of intervening halos (DM_{halos}) and the intergalactic medium (IGM; DM_{IGM}). Here, CGM refers to the gas found within dark matter halos including the intracluster medium of galaxy clusters, and the IGM refers to gas between galaxy halos.

Macquart et al. (2020) have demonstrated that the FRB population defines a cosmic DM–z relation that closely tracks the prediction of modern cosmology (Inoue 2004; Deng & Zhang 2014; Prochaska & Zheng 2019), i.e., the average cosmic DM is

$$\langle DM_{cosmic} \rangle = \int_0^{z_{host}} \bar{n}_e(z) \frac{c\,dz}{H(z)(1+z)^2} \qquad (2)$$

with $\bar{n}_e = f_d(z)\rho_b(z)/m_p(1 - Y_{He}/2)$, which is the mean density of electrons at redshift z. Here, m_p is the proton mass, $Y_{He} = 0.25$ is the mass fraction of helium (assumed doubly ionized in this gas), and $f_d(z)$ is the fraction of cosmic baryons in diffuse ionized gas, i.e., excluding dense baryonic phases such as stars and neutral gas (see Macquart et al. 2020 and the Appendix). $\rho_b(z) = \Omega_{b,0}\rho_{c,0}(1+z)^3$, $\rho_{c,0}$ is the critical density at $z = 0$, and $\Omega_{b,0}$ is the baryon energy density today relative to $\rho_{c,0}$. c is the speed of light in vacuum and $H(z)$ is the Hubble parameter. Immediately relevant to the study at hand, for FRB 190608, $\langle DM_{cosmic} \rangle \approx 100$ pc cm^{-3} at $z_{host} = 0.11778$.

Of the five FRBs in the "gold" sample of Macquart et al. (2020), FRB 190608 exhibits a DM_{cosmic} value well in excess of the average estimate for its redshift: $DM_{cosmic}/\langle DM_{cosmic} \rangle \approx 2$ based on the estimated contributions of $DM_{MW,halo}$ and DM_{host}. This is illustrated in Figure 1, which compares the measured $DM_{FRB} = 339.8$ pc cm^{-3} (Day et al. 2020) with the cumulative contributions from the Galactic ISM (taken as $DM_{MW,ISM} = 38$ pc cm^{-3}; Cordes & Lazio 2003), the Galactic halo (taken as $DM_{MW,halo} = 40$ pc cm^{-3}; Prochaska & Zheng 2019), and the average cosmic web (Equation (2)). These fall ≈ 160 pc cm^{-3} short of the observed value. Chittidi et al. (2020) estimate that the ISM in the host galaxy contributes $DM_{host,ISM} = 82 \pm 35$ pc cm^{-3} based on the observed Hβ emission measure and $DM_{host,halo} = 28 \pm 13$ pc cm^{-3} for the host galaxy's halo, thus nearly accounting for the deficit. The net DM_{host} is therefore taken here to be 110 ± 37 pc cm^{-3}.

While these estimates almost fully account for the large DM_{FRB}, several of them bear significant uncertainties (e.g., $DM_{MW,halo}$ and DM_{host}). Furthermore, we have assumed the average DM_{cosmic} value, a quantity predicted to exhibit significant variance from sightline to sightline (McQuinn 2014; Prochaska & Zheng 2019; Macquart et al. 2020). Therefore, in this work we
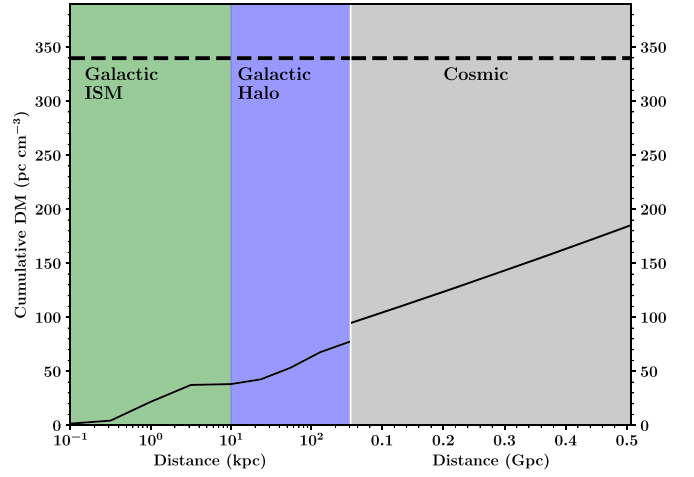

Figure 1. The cumulative FRB dispersion measure for FRB 190608. The dashed line corresponds to $DM_{FRB} = 339.8$ pc cm^{-3} reported for the FRB (Day et al. 2020), which is at the highest distance shown (≈ 0.5 Gpc). The solid curve is an estimate of the cumulative DM moving out from Earth toward the FRB. The Milky Way's ISM (green; model of Cordes & Lazio 2003) and halo (blue; model of Prochaska & Zheng 2019) together may contribute ≈ 100 pc cm^{-3}. If the foreground cosmic web (gray) contributes the expected average (Equation (2)), this adds an additional ≈ 100 pc cm^{-3} as modeled. Note that the horizontal axis is discontinuous at the halo–cosmic interface and this is the reason for a discontinuous cumulative DM. The difference between the solid and dashed lines at the FRB is ≈ 160 pc cm^{-3} and is expected to be attributed to the host galaxy and/or an above average contribution from the cosmic web (e.g., overdensities in the host galaxy foreground).

examine the galaxies and large-scale structure foreground to FRB 190608 to analyze whether $DM_{cosmic} \approx \langle DM_{cosmic} \rangle$ or whether there is significant deviation from the cosmic average. These analyses constrain several theoretical expectations related to $\langle DM_{cosmic} \rangle$ (e.g., McQuinn 2014; Prochaska & Zheng 2019). In addition, FRB 190608 exhibits a relatively large rotation measure (RM = 353 rad m^{-2}) and a large, frequency-dependent exponential tail ($\tau_{1.4Ghz} = 2.9$ ms) in its temporal pulse profile that corresponds to scatter-broadening (Day et al. 2020). We explore the possibility that these arise from foreground matter overdensities and/or galactic halos (similar to the analysis by Prochaska et al. 2019).

This paper is organized as follows. In Section 2, we present our data on the host and foreground galaxies and our spectral energy distribution (SED) fitting method for determining galaxy properties. In Section 3, we describe our methods and models in estimating the separate DM_{cosmic} contributions from intervening halos and the diffuse IGM. Section 4 explores the possibility of a foreground structure accounting for the FRB rotation measure and pulse width. Finally, in Section 5, we summarize and discuss our results. Throughout our analysis, we use cosmological parameters derived from the results of Planck Collaboration et al. (2016a).

2. Foreground Galaxies

2.1. The Data Set

FRB 190608 was detected and localized by the Australian Square Kilometre Array Pathfinder (ASKAP) to R.A. = $22^h16^m4\overset{s}{.}77$, decl. = $-07°53'53\overset{''}{.}7$ (Day et al. 2020), placing it in the outer disk of the galaxy J221604.90−075356.0 at $z = 0.11778$ (hereafter HG 190608) cataloged by the Sloan Digital Sky Survey (SDSS).

To search for nearby foreground galaxies, we obtained six $33'' \times 20''$ integral field unit (IFU) exposures (1800 s each) using the Keck Cosmic Web Imager (KCWI; Morrissey et al. 2018) in a mosaic centered at the host galaxy centroid. The IFU was used in the "large" slicer position with the "BL" grating, resulting in a spectral resolution $R_0 \sim 900$. The six exposures cover an approximately $1' \times 1'$ field around the FRB host. They were reduced using the standard KCWI reduction pipeline (Morrissey et al. 2018) with sky subtraction (see Chittidi et al. 2020 for additional details).

From the reduced cubes, we extracted the spectra of sources identified in the white-light images using the Source Extractor and Photometry (SEP) package (Bertin & Arnouts 1996; Barbary 2016). We set the detection threshold to 1.5 times the estimated rms intensity after background subtraction and specified a minimum source area of 10 pixels ($\sim$5 kpc at $z = 0.05$) to be a valid detection. Thirty sources were identified in this way across the six fields; none has an SDSS spectrum. SEP determines the spatial light profiles of the sources, and for each source it outputs major and minor axis values of a Gaussian fit. Using elliptical apertures with twice those linear dimensions, we extracted source spectra. We then determined their redshifts using the Manual and Automatic Redshifting Software (MARZ, Hinton et al. 2016). MARZ fits each spectrum with a template spectrum and determines the redshift corresponding to the maximum cross-correlation. Seven objects had unambiguous redshift estimates, whereas the rest did not show any identifiable line emission. Five of the seven objects with secure redshifts are at $z > z_{host}$ and are not discussed further. We observed two objects (R.A. $= 22^h16^m4\overset{s}{.}86$, decl. $= -7°53'44\overset{''}{.}16$ (J2000)) with a single strong emission feature at 4407 Å for one and 3908 Å for the other. MARZ reported high cross-correlations with its templates for when this feature was associated with either the [O II] 3727–3729 Å doublet (corresponding to $z < z_{FRB}$) or Lyα (corresponding to $z > 2$). There are no other discernible emission lines in the spectra. If we assume the emission line is indeed [O II], we can then measure the peak intensity of Hβ. Thus, in both spectra, the Hβ peak would be less than 0.02 times the [O II] peak intensity, which would imply an impossible metallicity. Thus we conclude that the features are likely Lyα and place these as galaxies at $z > 2.6$.

In the remaining 23 spectra, we detect no identifiable emission lines. Since we measure only weak continua (per-pixel signal-to-noise ratio < 1), if any, from the remaining 23 objects, we find it difficult to estimate the likelihood of their being foreground objects from synthetic colors.

We experimented with decreasing the minimum detection area threshold to 5 pixels. This increases the number of detected sources, but the additional sources, assuming they are actually astrophysical, do not have any identifiable emission lines. These sources are most likely fluctuations in the background.

To summarize, we found no foreground galaxy in the $1'$ sq. KCWI field. Assuming the halo mass function (HMF) derived from the Aemulus project (McClintock et al. 2019), the average number of foreground halos (i.e., for $z < z_{host}$ and in a $1' \times 1'$ field) between $2 \times 10^{10} M_\odot$ and $10^{16} M_\odot$ is 0.23; therefore, the absence of objects can be attributed to Poisson variance. This general conclusion remains valid even when we refine the expected number of foreground halos based on the inferred overdensities along the line of sight (see Section 3.2.2).

To expand the sample, we then queried the SDSS-DR16 database for all spectroscopically confirmed galaxies with impact parameters $b < 5$ Mpc (physical units) to the FRB sightline and $z < z_{host}$. This impact parameter threshold was chosen to encompass any galaxy or large-scale structure that might contribute to DM_{cosmic} along the FRB sightline. As the FRB is located in one of the narrow strips in the SDSS footprint, the query is spatially truncated in the northeastern direction. Effectively no object with $b \gtrsim 2.5$ Mpc in that direction was present in the query results because of this selection effect.

We further queried the SDSS database for all galaxies with photometric redshift estimates such that $z_{phot} - 2\delta z_{phot} < z_{host}$ and $z_{phot}/\delta z_{phot} > 1$. Here δz_{phot} is the error in z_{phot} reported in the database. We rejected objects that were flagged as cosmic rays or were suspected cosmic rays or CCD ghosts. None of these recovered galaxies lies within 250 kpc of the sightline as estimated from z_{phot}. However, several galaxies were found with $z_{phot} > z_{host}$ and $z_{phot} - 2\delta z_{phot} < z_{host}$ that can be within 250 kpc if their actual redshifts were closer to $z_{phot} - 2\delta z_{phot}$.

2.2. Derived Galaxy Properties

For each galaxy in the spectroscopic sample, we have estimated its stellar mass, $M_\star$, by fitting the SDSS *ugriz* photometry with an SED using CIGALE (Noll et al. 2009). We assumed, for simplicity, a delayed-exponential star formation history with no burst population, a synthetic stellar population prescribed by Bruzual & Charlot (2003), the initial mass function (IMF) of Chabrier (2003), dust attenuation models from Calzetti (2001), and dust emission templates from Dale et al. (2014), where the fraction of active galactic nuclei was capped at 20%. The models typically report a statistical uncertainty of $\lesssim$0.1 dex on $M_\star$ and star formation rate from the SED fitting, but we estimate systematic uncertainties are $\approx$2$\times$ larger. Table 1 lists the observed and derived properties for the galaxies.

Central to our estimates of the contribution of halos to the DM is an estimate of the halo mass, M_{halo}. A commonly adopted procedure is to estimate M_{halo} from the derived stellar mass, $M_\star$, by using the abundance matching technique. Here, we adopt the stellar-to-halo mass ratio (SHMR) of Moster et al. (2013), which also assumes the Chabrier IMF. Estimated halo masses of the foreground galaxies range from $10^{11} M_\odot$ to $\gtrsim 10^{12} M_\odot$.

2.3. Redshift Distribution of Foreground Galaxies

Figure 2 shows the distribution of impact parameters and spectroscopic redshifts for the foreground galaxies. There is a clear excess of galaxies at $z \sim 0.08$. Empirically, there are 50 galaxies within a redshift range $\Delta z = 0.005$ of $z = 0.0845$. A review of group and cluster catalogs of the SDSS (Yang et al. 2007; Rykoff et al. 2014), however, shows no massive collapsed structure ($M_{halo} > 10^{13} M_\odot$) at this redshift and within $b = 2.5$ Mpc of the sightline. The closest redMaPPer cluster at this redshift is at a transverse distance of 8.7 Mpc. However, we must keep in mind that the survey is spatially truncated in the northeastern direction and therefore we cannot conclusively rule out the presence of a nearby galaxy group or cluster. Nevertheless, the distribution suggests an overdensity of galaxies tracing some form of large-scale structure, e.g., a

Table 1
Observed and Derived Properties of the Spectroscopic Foreground Galaxies from SDSS[a]

R.A. (deg)	Decl. (deg)	u (mag)	g (mag)	r (mag)	i (mag)	z (mag)	Redshift	b (kpc)	$\log(M_*/M_\odot)$	$\log(M_{halo}/M_\odot)$
334.00914	−7.87554	18.73	17.54	16.98	16.63	16.37	0.09122	158	10.36	11.81
333.97368	−7.87678	19.28	17.87	16.95	16.50	16.20	0.08544	300	10.59	12.09
333.88476	−8.01812	18.48	17.39	16.92	16.72	16.59	0.02732	367	9.06	11.04
334.01930	−8.02294	18.31	16.58	15.74	15.38	15.13	0.06038	541	10.63	12.17
334.04856	−7.79251	19.89	17.99	17.05	16.63	16.19	0.07745	597	10.54	12.01
333.77207	−7.53690	19.79	17.99	17.51	17.24	17.01	0.02394	784	8.85	10.95
334.07667	−7.76554	19.43	18.24	17.39	16.96	16.61	0.08110	819	10.37	11.82
333.99058	−8.10044	19.97	18.48	17.88	17.47	17.30	0.06522	951	9.75	11.39
334.08866	−8.01256	18.95	18.38	17.29	16.84	16.56	0.11726	1050	10.91	12.79
334.12864	−8.08630	19.20	17.86	17.31	16.96	16.75	0.07096	1091	10.01	11.55

Note.
[a] This table is published in its entirety in the machine-readable format. Ten galaxies with the lowest impact parameters are shown here.

(This table is available in its entirety in machine-readable form.)
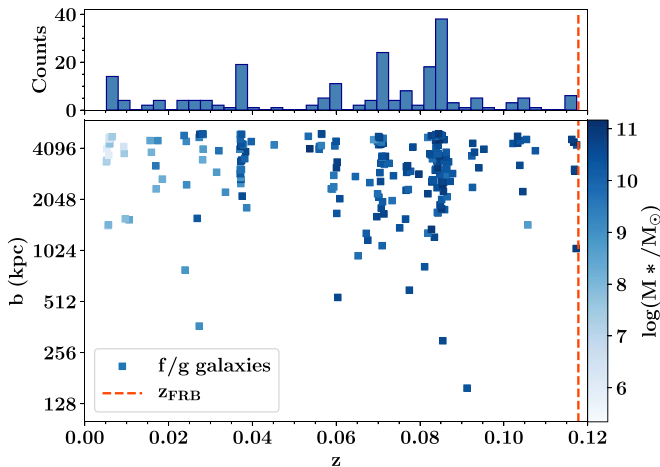
Figure 2. The spatial distribution of foreground galaxies. Bottom: a scatter plot of foreground galaxy redshifts, z, and impact parameters, b. The points are colored according to the estimated stellar masses. The red dashed line indicates the FRB host redshift. Top: a histogram of the redshifts. The "spikes" in the distribution, e.g., at $z \sim 0.08$, indicate overdensities in the underlying cosmic web structure.
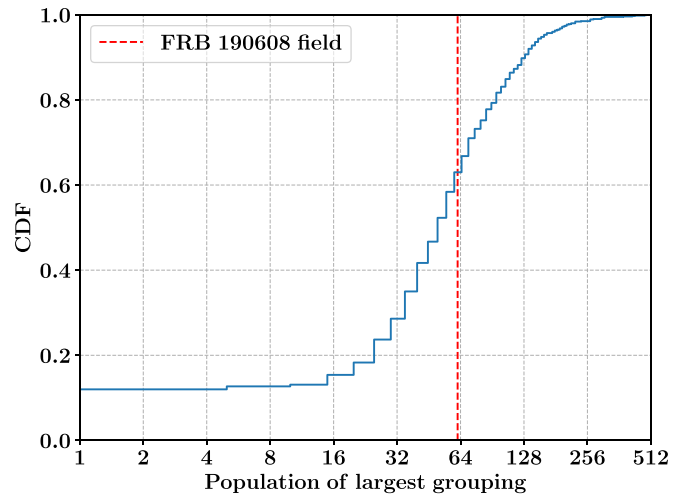

Figure 3. Grouping population sizes in SDSS fields. A cumulative histogram of the sizes of the most populous redshift groupings in 1000 random SDSS fields. Each field was searched for galaxies more massive than $10^{9.3} M_\odot$ with spectra within 5 Mpc of a sightline passing through the center. The groupings are computed using a mean-shift algorithm with bandwidth $\Delta z = 0.005$. Their centroids all lie between $z = 0.02$ and z_{host}. The most populous redshift grouping found in the FRB field at $z \sim 0.08$ is indicated by the red dashed line. At the 63rd percentile, the FRB field does not have rare overdensities in its foreground.

filament connecting this distant cluster to another (see Section 3.2.2).

To empirically assess the statistical significance of FRB 190608 exhibiting an excess of foreground galaxies (which would suggest an excess DM_{cosmic}), we performed the following analysis. First, we defined a grouping[12] of galaxies using a mean-shift clustering algorithm on the galaxy redshifts in the field, adopting a bandwidth Δz of 0.005 (≈ 3100 km s^{-1}). This generates a redshift centroid and the number of galaxies in a series of groupings for the field. For the apparent overdensity, we recover $z = 0.0843$ and $N = 62$ galaxies; this is the grouping with the highest cardinality in the field. We then generated 1000 random sightlines in the SDSS footprint and obtained the redshifts of galaxies with $z < z_{host}$ and with impact parameters $b < 5$ Mpc, restricting the sample to galaxies with $z > 0.02$ for computational expediency. We also

restricted the stellar masses to lie above $10^{9.3} M_\odot$ to account for survey completeness near $z = 0.08$. This provides a control sample for comparison with the FRB 190608 field.

Figure 3 shows the cumulative distribution of the number of galaxies in the most populous groupings in each field. We find that the FRB field's largest grouping is at the 63rd percentile, and therefore conclude that it is not a rare overdensity. It might, however, make a significant contribution to DM_{cosmic}, a hypothesis that we explore in the next section.

3. DM Contributions

This section estimates DM_{halos} and DM_{IGM}. For the sake of clarity, we make a distinction in the terminology we use to refer to the cosmic contribution to the DM estimated in two different ways. First, we name the difference between DM_{FRB} and the estimated host and Milky Way contributions $DM_{FRB,C}$,

---

[12] We avoid the use of group or cluster to minimize confusion with those oft used terms in astronomy.

i.e., $\mathrm{DM_{FRB,C}} = \mathrm{DM_{FRB}} - \mathrm{DM_{MW}} - \mathrm{DM_{host}} \approx 152$ pc cm^{-3}. Second, we shall henceforth use the term $\mathrm{DM_{cosmic}}$ to refer to the sum of $\mathrm{DM_{halos}}$ and $\mathrm{DM_{IGM}}$ semiempirically estimated from the foreground galaxies.

3.1. Foreground Halo Contribution to DM$_{cosmic}$

We first consider the DM contribution from halo gas surrounding foreground galaxies, $\mathrm{DM_{halos}}$. The four galaxies with $b < 550$ kpc all have estimated halo masses $M_{\mathrm{halo}} \leqslant 10^{12.2}\, M_{\odot}$. We adopt the definition of r_{vir} using the formula for average virial density from Bryan & Norman (1998), i.e., the average halo density enclosed within r_{vir} is

$$\begin{aligned} \rho_{\mathrm{vir}} &= (18\pi^2 - 82q - 39q^2)\rho_c \\ q &= \frac{\Omega_{\Lambda,0}}{\Omega_{m,0}(1+z)^3 + \Omega_{\Lambda,0}}. \end{aligned} \quad (3)$$

Here ρ_c is the critical density of the universe at redshift z and $\Omega_{\Lambda,0}$ is the dark energy density relative to $\rho_{c,0}$. Computing r_{vir} from the estimated halo masses, we find that only the halo with the smallest impact parameter at $z = 0.09122$ (i.e., first entry in Table 1) is intersected by the sightline. In the following, however, we will allow for uncertainties in M_{halo} and also consider gas out to $2r_{\mathrm{vir}}$. Nevertheless, we proceed with the expectation that $\mathrm{DM_{halos}}$ is small.

To derive the DM contribution from each halo, we must adopt a gas density profile and the total mass of baryons in the halo. For the former, we assume a modified Navarro–Frenk–White (NFW) baryon profile as described in Prochaska & Zheng (2019), with profile parameters $\alpha = 2$ and $y_0 = 2$. We terminate the profile at a radius r_{max}, given in units of r_{vir} (i.e., $r_{\mathrm{max}} = 1$ corresponds to r_{vir}). The gas composition is assumed to be primordial, i.e., 75% hydrogen and 25% helium by mass. For the halo gas mass, we define $M_{\mathrm{halo}}^b \equiv f_{\mathrm{hot}}(\Omega_b/\Omega_m)M_{\mathrm{halo}}$, with f_{hot} parameterizing the fraction of the total baryonic budget present within the halo as hot gas. For a halo that has effectively retained all of its baryons, a canonical value is $f_{\mathrm{hot}} = 0.75$, which allows for $\approx 25\%$ of the baryons to reside in stars, remnants, and neutral gas of the galaxy at its center (e.g., Fukugita et al. 1998). If feedback processes have effectively removed gas from the halo, then $f_{\mathrm{hot}} \ll 0.75$. For simplicity, we do not vary f_{hot} with halo mass but this fraction might well be a function of halo properties (e.g., Behroozi et al. 2010).

At present, we have only weak constraints on f_{hot}, α, and y_0, and we emphasize that our fiducial values are likely to maximize the DM estimate for a given halo (unless the impact parameter is $\ll r_{\mathrm{vir}}$). We therefore consider the estimated $\mathrm{DM_{halos}}$ to be an upper bound. However, we further note that the choice of r_{max}, which effectively sets the size of the gaseous halo, is largely arbitrary. In the following, we consider $r_{\mathrm{max}} = 1$ and 2.

The DM contribution of each foreground halo was computed by estimating the column density of free electrons intersecting the FRB sightline. Figure 4(a) shows the estimate of $\mathrm{DM_{halos}}$ for $r_{\mathrm{max}} = 1$. When $r_{\mathrm{max}} = 2$ (Figure 4(b)), the halo at $z = 0.09122$ (Table 1) contributes an additional ~ 10 pc cm^{-3} to the estimate of $\mathrm{DM_{halos}}$ from the extended profile. Furthermore, the halo at $z = 0.08544$ contributes ~ 10 pc cm^{-3} and the halo at $z = 0.06038$ contributes ~ 2 pc cm^{-3}.

In addition to the spectroscopic sample, we performed a similar analysis on the sample of galaxies with z_{phot} only. As

mentioned earlier, no galaxy in this sample was found within 250 kpc if their redshift was assumed to be z_{phot} and therefore their estimated contribution to $\mathrm{DM_{halos}}$ was null. However, if we assumed their redshifts were $z_{\mathrm{phot}} - 2\delta z_{\mathrm{phot}}$, we estimate a net DM contribution of ~ 30 pc cm^{-3} from four galaxies (Table 2). Their contribution decreases with increasing assumed redshift. At z_{host}, only the first two galaxies contribute and their net contribution is estimated to be ~ 13 pc cm^{-3}. A spectroscopic follow-up is necessary to pin down the galaxies' redshifts and therefore their DM contribution because they lie outside the field of view (FoV) of our KCWI data.

Using the aforementioned assumptions for the halo gas profile, we can compute the average contribution to $\langle \mathrm{DM_{cosmic}} \rangle$, i.e., $\langle \mathrm{DM_{halos}} \rangle$, by estimating the fraction of cosmic electrons enclosed in halos, $f_{e,\mathrm{halos}}(z)$. $\langle \mathrm{DM_{halos}} \rangle$ provides a benchmark that we may compare against $\mathrm{DM_{halos}}$. First, we find the average density of baryons found in halos between $10^{10.3}\, M_{\odot}$ and $10^{16}\, M_{\odot}$ using the Aemulus halo mass function (McClintock et al. 2019), i.e., $\rho_{b,\mathrm{halos}}(z)$. The ratio of this density to the cosmic matter density $\rho_b(z)$ is termed f_{halos}. Then, according to our halo gas model, $f_{e,\mathrm{halos}}(z)$ is

$$\begin{aligned} f_{e,\mathrm{halos}}(z) &= \frac{\bar{n}_{e,\mathrm{halos}}(z)}{\bar{n}_e(z)} = \frac{\rho_{b,\mathrm{halos}}(z)f_{\mathrm{hot}}}{\rho_b(z)f_d(z)} \\ &= f_{\mathrm{halos}}(z)\frac{f_{\mathrm{hot}}}{f_d(z)}. \end{aligned} \quad (4)$$

Lastly, we relate $\langle \mathrm{DM_{halos}} \rangle = f_{e,\mathrm{halos}} \times \langle \mathrm{DM_{cosmic}} \rangle$. The dashed lines in Figure 4 represent $\langle \mathrm{DM_{halos}} \rangle$, and we note that $\mathrm{DM_{halos}}$ for the FRB sightline is well below this value at all redshifts.

There are two major sources of uncertainty in estimating $\mathrm{DM_{halos}}$. First, stellar masses are obtained from SED fitting and have uncertainties of the order of 0.1 dex. In terms of halo masses, this translates to an uncertainty of ~ 0.15 dex if the mean SHMR is used. Second, there is scatter in the SHMR which is also a function of the stellar mass. Note that the intervening halos have stellar masses $\sim 10^{10.6}\, M_{\odot}$. This corresponds to an uncertainty in the halo mass of ~ 0.25 dex (Moster et al. 2013). In Figure 4, we have varied stellar masses by 0.1 dex and have depicted the variation in $\mathrm{DM_{halos}}$ through the shaded regions. If, instead, we varied the stellar masses by 0.16 dex, thus mimicking a variation in halo masses by nearly 0.25 dex, the scatter increases by roughly 10 pc cm^{-3} in Figure 4(a) and by about 20 pc cm^{-3} in Figure 4(b) at $z = 0.11778$.

For the remainder of our analysis, we shall use the estimate for $\mathrm{DM_{halos}}$ corresponding to $r_{\mathrm{max}} = 1$, i.e., $\mathrm{DM_{halos}} = 12$ pc cm^{-3} and is bounded between 7 pc cm^{-3} and 28 pc cm^{-3}, while bearing in mind that it may be roughly twice as large if the radial extent of halo gas exceeds r_{vir}. For the galaxies with photometric redshifts only, we shall adopt z_{phot} and thus estimate no contribution to $\mathrm{DM_{halos}}$.

3.2. DM$_{IGM}$ and DM$_{cosmic}$

We now proceed to estimate the other component of $\mathrm{DM_{cosmic}}$, $\mathrm{DM_{IGM}}$, the contribution from diffuse gas outside halos. In this section, we discuss two approaches to estimating $\mathrm{DM_{IGM}}$.

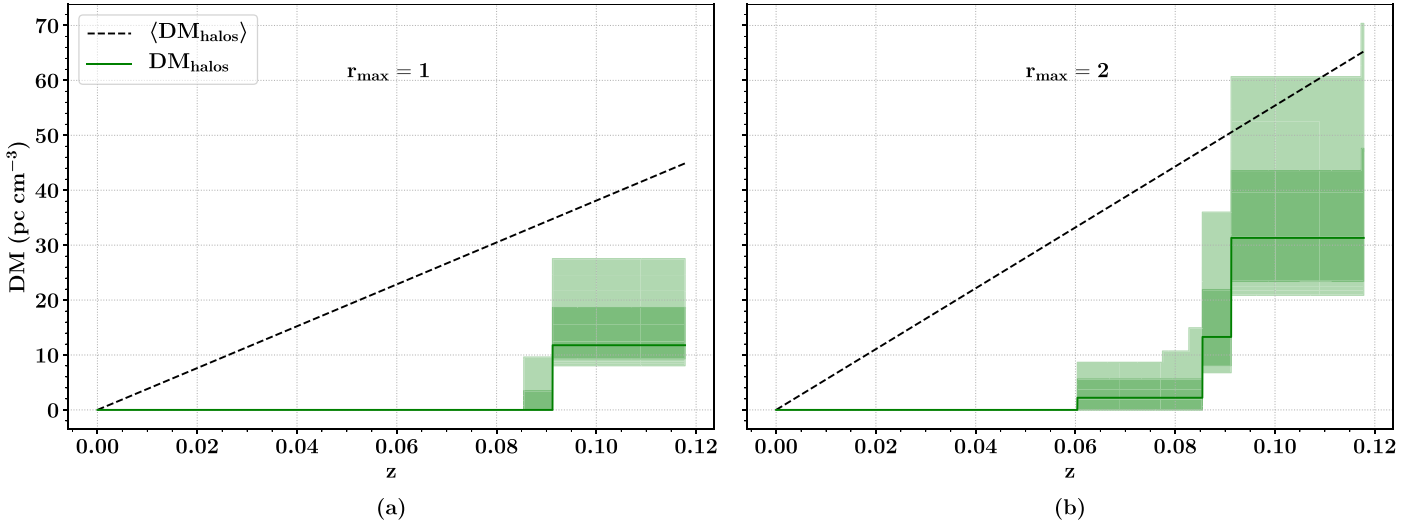1. The diffuse IGM is assumed to be uniform and isotropic. This implies that its DM contribution is completely

Figure 4. DM_{halos} vs. redshift. The black line represents $\langle DM_{halos} \rangle$, i.e., the average DM from halos using the Aemulus halo mass function (ignoring the IGM). The solid green line is our estimate of DM_{halos}, the DM contribution from intervening halos of galaxies found in SDSS and assuming a hot gas fraction $f_{hot} = 0.75$. The dark green shaded region is obtained by varying the stellar masses of each of the intervening halos by 0.1 dex, which modulates the adopted halo mass. This is representative of the uncertainty in DM propagated from stellar mass estimation. The lighter green shaded region is obtained by similarly varying the stellar masses by 0.16 dex and it is representative of the uncertainty in DM propagated from the scatter in the SHMR. This calculation was performed for two values of the dimensionless radial extent of the halo's matter distribution, r_{max}: 1 (left) and 2 (right). Using the central measures of stellar mass and the SHMR, the intervening galaxies contribute DM_{halos} less than the expected cosmic average, $\langle DM_{halos} \rangle$, and do not exceed 50 pc cm^{-3}.

determined by cosmology and our assumptions for DM_{halos}. This is equivalent to estimating the cosmic average of the IGM contribution, $\langle DM_{IGM} \rangle$.

2. Owing to structure in the cosmic web, the IGM is not assumed to be uniform. We infer the 3D distribution of the cosmic web using the galaxy distribution and then use this to compute DM_{IGM}.

We consider each of these in turn.

3.2.1. $\langle DM_{IGM} \rangle$

Approach 1 is an approximation of DM_{IGM}. We define

$$\langle DM_{IGM} \rangle = \langle DM_{cosmic} \rangle - \langle DM_{halos} \rangle. \quad (5)$$

Naturally, $\langle DM_{IGM} \rangle$ depends on redshift and on our parameterization of $\langle DM_{halos} \rangle$, i.e., on f_{hot} and r_{max}. At $z = z_{host}$ for $f_{hot} = 0.75$ and $r_{max} = 1$, $\langle DM_{IGM} \rangle \approx 54$ pc cm^{-3}, i.e., about 54% of $\langle DM_{cosmic} \rangle$.

Adopting this value of $\langle DM_{IGM} \rangle$, we can estimate DM_{cosmic} toward FRB 190608 by combining it with our estimate of DM_{halos} (Figure 1). This is presented as the blue, shaded curve in Figure 5 using our fiducial estimate for DM_{halos} ($f_{hot} = 0.75$, $r_{max} = 1$). This DM_{cosmic} estimate is roughly 90 pc cm^{-3} less than $DM_{FRB,C}$, and the discrepancy would be larger if one adopted a smaller $DM_{MW,halo}$ value than 40 pc cm^{-3} (e.g., Keating & Pen 2020). We have also computed DM_{cosmic} for different combinations of f_{hot} and r_{max} and show the results in Figure 6.

First, we note that the DM_{cosmic} estimate is always lower than $DM_{FRB,C}$. Second, it is not intuitive that the estimate is closer to $DM_{FRB,C}$ when $f_{hot} \approx 0$ (i.e., $DM_{halos} \approx 0$). This arises from our definition of $\langle DM_{IGM} \rangle$, i.e., $f_{hot} = 0$ implies $\langle DM_{halos} \rangle = 0$ or $\langle DM_{IGM} \rangle = \langle DM_{cosmic} \rangle$. As $\langle DM_{cosmic} \rangle = 100$ pc cm^{-3} is independent of f_{hot} and r_{max}, the estimate is close to $DM_{FRB,C}$. For all higher f_{hot}, $\langle DM_{IGM} \rangle$ is smaller and DM_{halos} is insufficient to add up to $DM_{FRB,C}$. In summary, DM_{halos} is consistently lower

than $\langle DM_{halos} \rangle$ for the parameter range we explored. This results in DM_{cosmic} thus estimated being systematically lower than $DM_{FRB,C}$.

3.2.2. Cosmic Web Reconstruction

As described in Section 3.1, the localization of FRB 190608 to a region with SDSS coverage enables modeling of the DM contribution from individual halos along the line of sight. It also invites the opportunity to consider cosmic gas residing within the underlying, large-scale structure. Theoretical models predict shock-heated gas within the cosmic web as a natural consequence of structure formation (Cen & Ostriker 1999; Davé et al. 2001), and indeed FRBs offer one of the most promising paths forward in detecting this elusive material (Macquart et al. 2020).

Using the SDSS galaxy distribution within 400′ of the FRB sightline, we employed the Monte Carlo Physarum Machine (MCPM) cosmic web reconstruction methodology introduced by Burchett et al. (2020) to map the large-scale structure intercepted by the FRB sightline. Briefly, the slime mold-inspired MCPM algorithm finds optimized network pathways between galaxies (analogous to food sources for the Physarum slime mold) in a statistical sense to predict the putative filaments in which they reside. The galaxies themselves occupy points in a 3D space determined by their sky coordinates and the luminosity distances indicated by their redshifts. At each galaxy location, a simulated chemo-attractant weighted by the galaxy mass is emitted at every time step. Released into the volume are millions of simulated slime mold "agents," which move at each time step in directions preferentially toward the emitted attractants. Thus, the agents eventually reach an equilibrium pathway network, producing a connected 3D structure that represents the putative filaments of the cosmic web. The trajectories of the agents are aggregated over hundreds of time steps to yield a "trace," which in turn acts as a proxy for the local density at each point in the volume (see Burchett et al. 2020 for further details).

Table 2
SDSS Galaxies with Photometric Redshifts That Potentially Contribute to DM_{halos}

R.A. (deg)	Decl. (deg)	Separation from FRB (arcmin)	u (mag)	g (mag)	r (mag)	i (mag)	z (mag)	z_{phot}	δz_{phot}
334.01251	−7.88616	0.84	22.09	20.41	19.56	19.34	18.94	0.21	0.06
334.03281	−7.90426	0.86	23.62	22.18	21.25	20.94	20.22	0.27	0.12
334.03590	−7.88558	1.22	22.89	22.33	21.31	21.08	19.63	0.34	0.13
334.00943	−7.87979	1.26	21.00	20.04	19.40	19.16	18.95	0.15	0.04
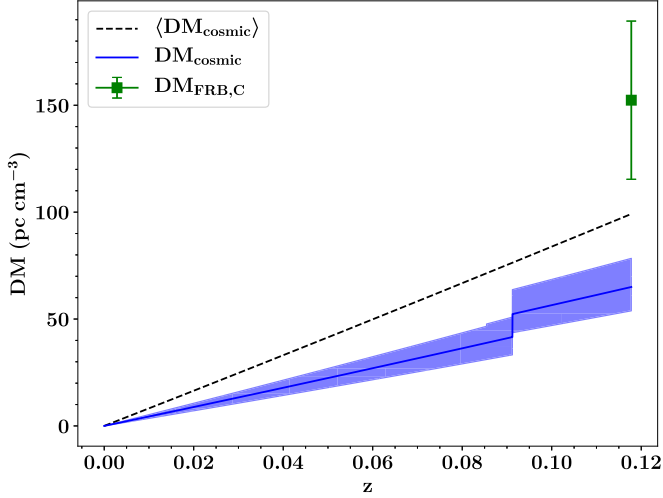
Figure 5. DM_{cosmic} vs. redshift. The solid blue line corresponds to $DM_{cosmic} = DM_{halos} + \langle DM_{IGM} \rangle$ with $f_{hot} = 0.75$ and $r_{max} = 1$. The shaded region represents the quadrature sum of uncertainties in DM_{halos} (allowing for 0.1 dex variation in stellar mass) and the IGM (taken to be 20% of DM_{IGM}). The green point is $DM_{FRB,C}$ (i.e., $DM_{FRB} - DM_{MW} - DM_{host}$). The error bars correspond to the uncertainty in DM_{host}, which is 37 pc cm^{-3}. The black line represents $\langle DM_{cosmic} \rangle$.
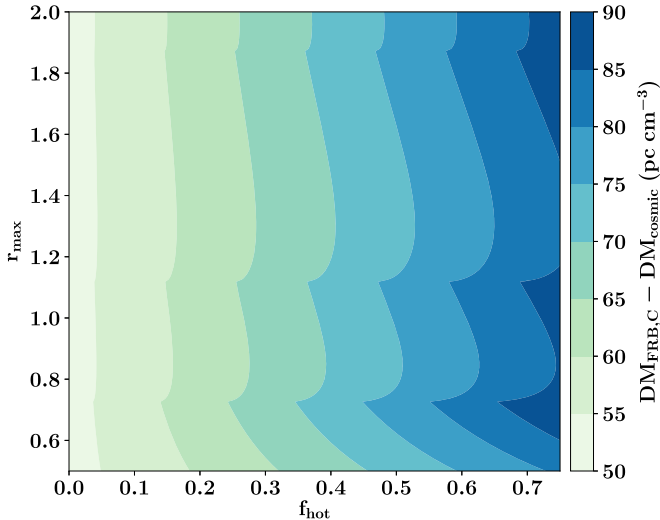
Figure 6. DM_{cosmic} compared to $DM_{FRB,C}$ as a function of halo model parameters. Here, DM_{cosmic} is defined as $DM_{halos} + \langle DM_{IGM} \rangle$ and depends on two key parameters, f_{hot} and r_{max}. f_{hot} is the fraction of baryonic matter present as hot gas in halos, and r_{max} is the radial extent in units of r_{vir} up to which baryons are present in the halo. At low f_{hot} and r_{max} values, DM_{halos} is small and $DM_{cosmic} \approx \langle DM_{IGM} \rangle \approx \langle DM_{cosmic} \rangle$. Toward higher f_{hot} and r_{max} values, $\langle DM_{IGM} \rangle$ decreases and DM_{halos} increases. However, $DM_{halos} < \langle DM_{halos} \rangle$. Thus DM_{cosmic} decreases further compared to $DM_{FRB,C}$. In summary, the fact that DM_{cosmic} estimated in this way is small is a reflection of the lower than average contribution from DM_{halos}.

Our reconstruction of the structure intercepted by our FRB sightline is visualized in Figure 7. The MCPM methodology simultaneously offers the features of (1) producing a continuous 3D density field defined even relatively far away from galaxies on megaparsec scales and (2) tracing anisotropic filamentary structures on both large and small scales.

With the localization of FRB 190608 both in redshift and projected sky coordinates, we retrieved the local density as a function of redshift along the FRB sightline from the MCPM-fitted volume. The SDSS survey is approximately complete to galaxies with $M_\star \gtrsim 10^{10.0}\, M_\odot$, which translates via abundance matching (Moster et al. 2013) to $M_{halo} \gtrsim 10^{11.5}\, M_\odot$. Therefore, we only used galaxies and halos above these respective mass limits in our MCPM fits for the SDSS and Bolshoi–Planck data sets. This prevents us from extending the redshift range of our analysis beyond 0.1, because going further would require a higher mass cutoff and therefore a much sparser sample of galaxies on which to perform the analysis. At the lower end of the redshift scale, there are fewer galaxies more massive than $10^{10.0}\, M_\odot$ (see Figure 2) and therefore the MCPM fits are limited to $z > 0.018$. To translate the MCPM density metric ρ_{Phys} to a physical overdensity $\delta\rho/\rho_m$, we applied MCPM to the dark matter-only Bolshoi cosmological simulation, where the matter density ρ_m is known at each point. Rather than galaxies, we fed the MCPM locations and masses of dark matter halos (Behroozi et al. 2013). We then calibrated ρ_{Phys} to ρ/ρ_m as detailed by Burchett et al. (2020). This produces a mapping to physical overdensity, albeit less tightly constrained than that of Burchett et al. (2020) due to the sparser data set we employ here. For densities $\rho \gtrsim \rho_m$, we estimate a roughly order-of-magnitude uncertainty in ρ/ρ_m derived along the line of sight. Figure 8 shows the density relative to the average matter density as a function of redshift.

The electron number density $n_e(z)$ is obtained by multiplying $\bar{n}_e(z)$ from Equation (2) by the MCPM estimate for ρ/ρ_m. Last, we integrate n_e to estimate DM_{IGM}^{slime} and recover $DM_{IGM}^{slime} = 78$ pc cm^{-3} for the redshift interval $z = [0.018, 0.1]$ (see Figure 9(a)). DM_{IGM}^{slime} is nearly double the value of $\langle DM_{IGM} \rangle$ at $z = 0.1$ assuming $f_{hot} = 0.75$ and $r_{max} = 1$.

The Bolshoi–Planck mapping from the trace densities to physical overdensity includes an uncertainty of ∼0.5 dex in each trace density bin. To estimate the uncertainty in DM_{IGM}^{slime}, we first identify the peaks in Figure 8. For all pixels within the FWHM of each peak, we vary the relative density by a factor that does not exceed 0.5 dex. This factor is drawn from a uniform distribution in log space. Each peak was assumed to be independent and thus varied by a different factor, and DM_{IGM}^{slime} was recomputed. From 100,000 such realizations of DM_{IGM}^{slime}, we estimated a probability density function (PDF) (Figure 9(b)). The 25th and 75th percentiles of this distribution are 75 pc cm^{-3} and 110 pc cm^{-3}, respectively, and the median value is 91 pc cm^{-3}. For the redshift intervals excluded, we
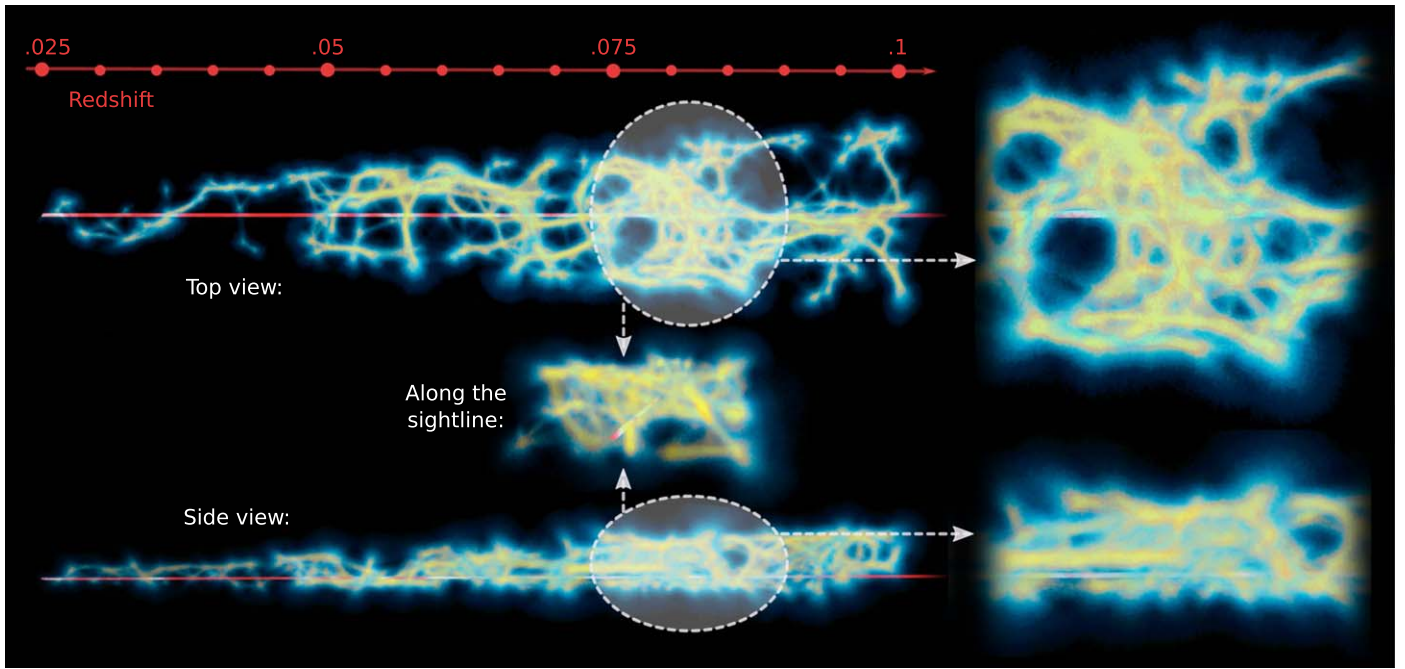
Figure 7. A 3D model of the cosmic web in physical coordinates reconstructed using the MCPM. Left, top: the red line passing through the web represents the FRB sightline where light is assumed to travel from right to left. The cosmic web reconstruction (Elek et al. 2020) is shown color-coded by the steady-state Physarum particle trace density (yellow being high and black being low). The red line with ticks along the top shows the horizontal scale of the reconstruction in redshift. In the vertical direction, the reconstructed region of the web spans an angular diameter of 800′ on the sky. Left, bottom: a rotated view of the reconstruction. The FRB sightline falls within a narrow strip of the SDSS footprint, and the vertical size in the side view is smaller than that in the top view. Left, center: a view along the sightline (which is again visible in red) of a high-density region enclosed by the translucent circles in the top and side views. Right: two close-up views of the locations indicated by the circles on the left.
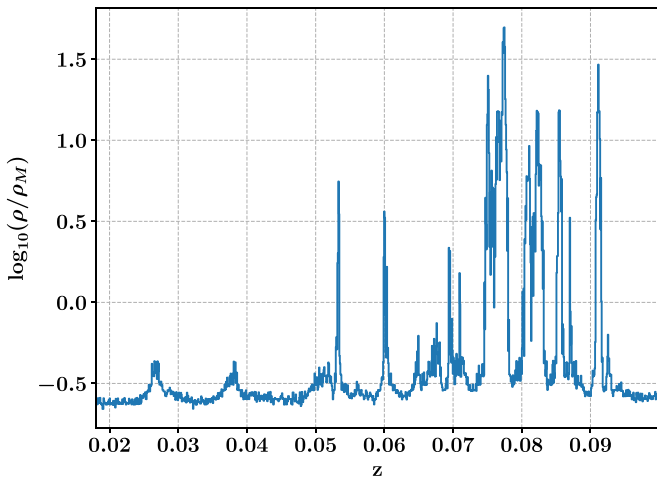
Figure 8. Estimate of cosmic web density from MCPM. We show the MCPM-derived cosmic overdensity as a function of redshift along the line of sight to FRB 190608. We first produced our cosmic web reconstruction from SDSS galaxies within 400′ of the sightline and then calibrated the MCPM trace (see text) with the cosmic matter density from the Bolshoi–Planck simulation. Note that there are apparently no galaxy halos ($\rho > 100\rho_m$) captured here, although several density peaks arise from large-scale filamentary structures. We in turn use the 3D map from MCPM to model the diffuse IGM gas and produce DM_{IGM} estimates.

assume $n_e = \bar{n}_e$ and estimate an additional 16 pc cm^{-3} to DM_{IGM} (8 pc cm^{-3} for $z < 0.018$ and 8 pc cm^{-3} for $z > 0.1$), increasing DM_{IGM} to 94 pc cm^{-3}. This is justified by comparing Figures 2 and 8 to assess that there are no excluded overdensities that can contribute more than a few pc cm^{-3} over the average

value. In conclusion, we estimate $DM_{IGM} = 94$ pc cm^{-3}, with the 25th and 75th percentile bounds being 91 and 126 pc cm^{-3}.

With detailed knowledge of the IGM matter density, one can consider defining the boundary of a halo more precisely. A natural definition for the halo radius would be where the halo gas density and the IGM density are identical. Therefore, we tested whether the r_{max} obtained would significantly differ from the chosen value of unity, and thus produce substantially different DM_{halos}, for the intervening halos. We estimated r_{max} using this condition by setting the IGM density as the value obtained from the MCPM model at each halo redshift, yielding $r_{max} \approx 1.3–2.2$ for the halos. DM_{halos} estimated using these r_{max} values for the halos is ≈ 30 pc cm^{-3} because only the first two halos in Table 1 contribute. This is only slightly higher than the upper bound obtained previously for $r_{max} = 1$, and therefore we choose to continue with the value of DM_{halos} initially estimated using $r_{max} = 1$. Finally, our cosmic web reconstruction from the MCPM algorithm also allows us to refine our estimate of expected intervening galaxy halos in the KCWI FoV, $\langle n_{halos}^{KCWI} \rangle = 0.23$, presented in Section 2.1. Given the inferred overdensity as a function of redshift along the line of sight, $\rho/\rho_m(z)$, and the comoving volume element given by the KCWI FoV as a function of redshift, $dV(z)$, we can then just scale $\langle n_{halos}^{KCWI} \rangle$ by $\alpha \equiv \frac{\int (\rho / \rho_m(z)) \, dV(z) \, dz}{\int dV(z) \, dz}$. In our case, we have obtained $\alpha = 1.66$, and then our refined $\langle n_{halos}^{KCWI} \rangle = 0.38$. This number is still small and thus fully consistent with a lack of intervening halos found in the KCWI FoV.
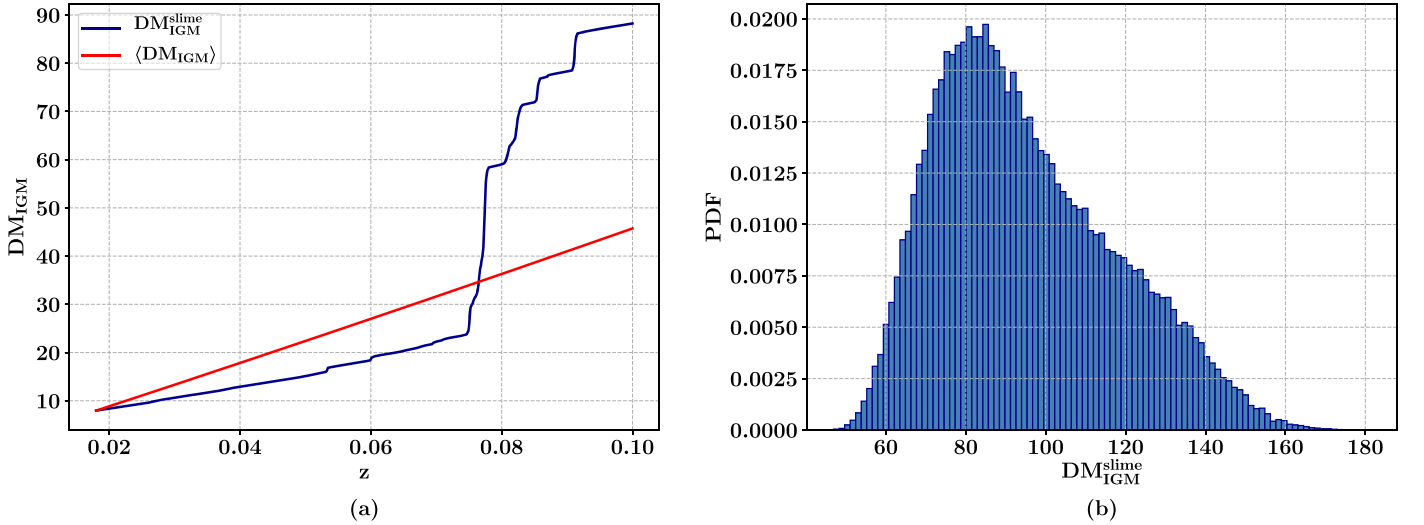
(a)

(b)

Figure 9. DM_{IGM}^{slime} from MCPM density estimate. Left: a comparison of DM_{IGM} obtained from the MCPM analysis (blue) and $\langle DM_{IGM} \rangle$ (red) assuming $f_{hot} = 0.75$ and $r_{max} = 1$. Below $z = 0.018$, where the MCPM density estimate is not available, DM_{IGM}^{slime} is assumed to be equal to $\langle DM_{IGM} \rangle$. At $z = 0.1$, DM_{IGM}^{slime} is nearly twice $\langle DM_{IGM} \rangle$. Right: the PDF of DM_{IGM}^{slime} estimated after accounting for the uncertainties in the Bolshoi–Planck mapping from particle trace densities to physical overdensities. The FWHM of each density peak is independently varied by a factor within 0.5 dex and a cumulative DM is computed. This estimate of the PDF is obtained from 100,000 realizations of DM_{IGM}^{slime}. $DM_{IGM}^{slime} = 88$ pc cm^{-3} for $z \leqslant 0.1$, and its distribution is asymmetric with a standard deviation of ~ 15 pc cm^{-3}.

4. Cosmic Contributions to the Rotation Measure and Temporal Broadening

We briefly consider the potential contributions of foreground galaxies to FRB 190608's observed temporal broadening and rotation measure. As is evident in Table 1, there is only a single halo within 200 kpc of the sightline with $z \leqslant z_{host}$. It has redshift $z = 0.09122$ and an estimated halo mass $M_{halo} = 10^{12} \, M_{\odot}$.

FRB 190608 exhibits a large, frequency-dependent pulse width $\tau = 3.3$ ms at 1.28 GHz (Day et al. 2020), which exceeds the majority of previously reported pulse widths (Petroff et al. 2016). Pulses are broadened when interacting with turbulent media. While we expect a scattering pulse width much smaller than a few milliseconds from the diffuse IGM alone (Macquart & Koay 2013), we consider the possibility that the denser halo gas at $z = 0.09122$ contributes significantly to FRB 190608's intrinsic pulse profile. Here, we estimate the extent of such an effect, emphasizing that the geometric dependence of scattering greatly favors gas in intervening halos as opposed to the host galaxy.

Assuming the density profile as described in Section 3.1 (extending to $r_{max} = 1$), the maximum electron density ascribed to the halo is at its impact parameter $b = 158$ kpc: $n_e \sim 10^{-4}$ cm^{-3}. Note that b is much greater than the impact parameter of the foreground galaxy of FRB 181112 (29 kpc, Prochaska et al. 2019) and indeed that of the host or the Milky Way with FRB 190608's sightline. The entire intervening halo can be thought of effectively as a "screen" whose thickness is the length the FRB sightline intersects with the halo, $\Delta L = 265$ kpc. We assume that the turbulence is described by a Kolmogorov distribution of density fluctuations with an outer scale $L_0 = 1$ pc. This choice of L_0 arises from assuming that stellar activity is the primary driving mechanism. To get an upper bound on the pulse width produced, we also assume that the electron density is equal to 10^{-4} cm^{-3} for the entire length of the intersected sightline. Following the scaling relation in

Equation (1) from Prochaska et al. (2019), we obtain

$$\tau_{1.4 \, GHz} < 0.028 \text{ ms } \alpha^{12/5} \left(\frac{n_e}{10^{-4} \text{ cm}^{-3}} \right)^{12/5}$$
$$\times \left(\frac{\Delta L}{265 \text{ kpc}} \right)^{6/5} \left(\frac{L_0}{1 \text{ pc}} \right)^{-4/5}. \tag{6}$$

Here, α is a dimensionless number that encapsulates the rms amplitude of the density fluctuations and the volume-filling fraction of the turbulence. It is typically of order unity. We note that our chosen value of L_0 presents an upper limit on the scattering timescale. Were $L_0 \gg 1$ pc (e.g., if driven by jets from active galactic nuclei), $\tau \ll 0.03$ ms. The observed scattering timescale exceeds our conservative upper bound by two orders of magnitude. One would require $n_e > 6 \times 10^{-4}$ cm^{-3} to produce the observed pulse width. This exceeds the maximum density estimation through the halo, even for the relatively flat and high f_{hot} assumed. We thus conclude that the pulse broadening for FRB 190608 is not dominated by intervening halo gas.

FRB 190608 also has a large estimated $RM_{FRB} = 353 \pm 2$ rad m^{-2} (Day et al. 2020). We may estimate the RM contributed by the intervening halo, under the assumption that its magnetic field is characterized by the magnetic fields of equipartition strength in galaxies ($\sim 10 \, \mu G$) (Basu & Roy 2013). We note that this exceeds the upper limit imposed on gas in the halo intervening along our sightline to FRB 181112 (Prochaska et al. 2019).

We estimate

$$RM_{halos} = 0.14 \text{ rad m}^{-2} \left(\frac{B_{\parallel}}{10 \, \mu G} \right) \left(\frac{\Delta L}{265 \text{ kpc}} \right)$$
$$\times \left(\frac{n_e}{10^{-4} \text{ cm}^{-3}} \right) \tag{7}$$

Table 3
Contributions to DM_{FRB} from Foreground Components

Component	Subcomponent	Notation	Value (pc cm^{-3})	Comments
Host galaxy	ISM	$DM_{host,ISM}$	47–117	From Chittidi et al. (2020)
	Halo	$DM_{host,halo}$	15–41	From Chittidi et al. (2020)
Foreground cosmos	Intervening halos	DM_{halos}	7–28[a]	Using SDSS spectroscopic galaxies and 0.16 dex scatter in M^*
		$\langle DM_{halos} \rangle$	45[a]	Average assuming the Aemulus HMF and Planck 15 cosmology
	Diffuse IGM	DM_{IGM}	91–126	25th and 75th percentiles using the MCPM method
		$\langle DM_{IGM} \rangle$	54[a]	Average assuming the Aemulus HMF and Planck 15 cosmology
Milky Way	ISM	$DM_{MW,ISM}$	38	From Cordes & Lazio (2003)
	Halo	$DM_{MW,halo}$	40	From Prochaska & Zheng (2019)

Note.
[a] Assuming $f_{hot} = 0.75$ and $r_{max} = 1$.

and conclude that it is highly unlikely that the RM contribution from intervening halos dominates the observed quantity.

5. Concluding Remarks

To summarize, we have created a semiempirical model of the matter distribution in the foreground universe of FRB 190608 using spectroscopic and photometric data from the SDSS database and our own KCWI observations. We modeled the virialized gas in intervening halos using a modified NFW profile and used the MCPM approach to estimate the ionized gas density in the IGM. Table 3 summarizes the estimated DM contributions from each of the individual foreground components. Adding $\langle DM_{halos} \rangle$ and DM_{IGM} for this sightline, we infer $DM_{cosmic} = 98$–154 pc cm^{-3}, which is comparable to $\langle DM_{cosmic} \rangle = 100$ pc cm^{-3}. The majority of DM_{cosmic} is accounted for by the diffuse IGM, implying that most of the ionized matter along this sightline is not in virialized halos. We found only four galactic halos within 550 kpc of the FRB sightline and only one within 200 kpc. We found no foreground object in emission from our $\sim 1'$ sq. KCWI coverage and no galaxy group or cluster having an impact parameter of less than its virial radius with our FRB sightline.

We also find it implausible that the foreground structures are dense enough to account for either the pulse broadening or the large rotation measure of the FRB. We expect that the progenitor environment and the host galaxy together are the likely origins of both Faraday rotation and turbulent scattering of the pulse (discussed in further detail by Chittidi et al. 2020).

The results presented here are not the first attempt to measure DM_{cosmic} along FRB sightlines by accounting for density structures. Li et al. (2019) estimated DM_{cosmic} (termed DM_{IGM} in their paper) for five FRB sightlines, making use of the Two Micron All Sky Survey Redshift Survey group catalog (Lim et al. 2017) to infer the matter density field along their lines of sight. They assumed NFW profiles around each identified group. This enabled them to estimate the DM contribution from intervening matter for FRBs with low DM ($DM_{cosmic} + DM_{host} < 100$ pc cm^{-3}).

Our approach differs in the methods used to estimate DM_{cosmic}. The precise localization of FRB 190608 allows us to estimate DM_{halos} and DM_{IGM} separately. Li et al. (2019) were limited by the large uncertainties ($\sim 10'$) in the FRB position, and therefore their estimates of $\langle DM_{cosmic} \rangle$ depended on the assumed host galaxy within the localization regions. Furthermore, the MCPM model estimates the cosmic density field, and thus the ionized gas density of the IGM, due to large-scale filamentary structure. We note that our estimate of n_e from the MCPM model in overdense regions is similar to their reported values (10^{-6}–10^{-5} cm^{-3}). This naturally implies that our DM_{cosmic} estimates are of the same order of magnitude around $z = 0.1$ as their estimate. Together with the results presented by Chittidi et al. (2020), our study represents the first of its kind: an observationally driven, detailed DM budgeting along a well-localized FRB sightline. We have presented a framework for using FRBs as quantitative probes of foreground ionized matter. Although aspects of this framework carry large uncertainties at this juncture, the methodology should become increasingly precise as this nascent field of study matures. For instance, our analysis required spectroscopic data across a wide area (i.e., a few square degrees) around the FRB, which enabled us to constrain the individual contributions of halos and also to model the cosmic structure of the foreground IGM. An increase in sky coverage and depth of spectroscopic surveys would enable the use of cosmic web mapping tools such as the MCPM estimator with higher precision and on more FRB sightlines. Upcoming spectroscopic instruments such as DESI and 4MOST will map out cosmic structure in greater detail and will, no doubt, aid in the use of FRBs as cosmological probes of matter.

We expect FRBs to be localized more frequently in the future, thanks to continued improvements in backends with high time resolution and real-time detection systems for radio interferometers. One can turn the analysis around and use the larger set of localized FRBs to constrain models of the cosmic web in a region and possibly perform tomographic reconstructions of filamentary structure. Alternatively, by accounting for the DM contributions of galactic halos and diffuse gas, one

may constrain the density and ionization state of matter present in intervening galactic clusters or groups. Understanding the cosmic contribution to the FRB DMs can also help to constrain progenitor theories by setting upper limits on the amount of DM arising from the region within a few parsecs of the FRB. We are at the brink of a new era of cosmology with new discoveries and constraints coming from FRBs.

Appendix
Cosmic Diffuse Gas Fraction

Central to an estimate of DM_{cosmic} is the fraction of baryons that are diffuse and ionized in the universe, f_d. We have presented a brief discussion of f_d in previous works (Prochaska & Zheng 2019; Macquart et al. 2020) and provide additional details and an update here.

To estimate $f_d(z)$, we work backwards by defining and estimating the cosmic components that do not contribute to DM_{cosmic}. These are

1. Baryons in stars, ρ_{stars}. This quantity is estimated from galaxy surveys and inferences of the stellar initial mass function (Madau & Dickinson 2014).
2. Baryons in stellar remnants and brown dwarfs, $\rho_{remnants}$. This quantity was estimated by Fukugita (2004) to be $\approx 0.3\rho_{stars}$ at $z = 0$. We adopt this fraction for all cosmic time.
3. Baryons in neutral atomic gas, ρ_{HI}. This is estimated from 21 cm surveys.
4. Baryons in molecular gas, ρ_{H_2}. This is estimated from CO surveys.

One could also include the small contributions from heavy elements, but we ignore this because it is a value smaller than the uncertainty in the dominant components.

Altogether, we define

$$f_d \equiv 1 - \frac{\rho_{stars}(z) + \rho_{remnants}(z) + \rho_{ISM}(z)}{\rho_b(z)} \qquad (A1)$$

where we have defined $\rho_{ISM} \equiv \rho_{HI} + \rho_{H_2}$. Fukugita (2004) has estimated $\rho_{ISM}/\rho_{stars} \approx 0.38$ at $z = 0$, and galaxy researchers
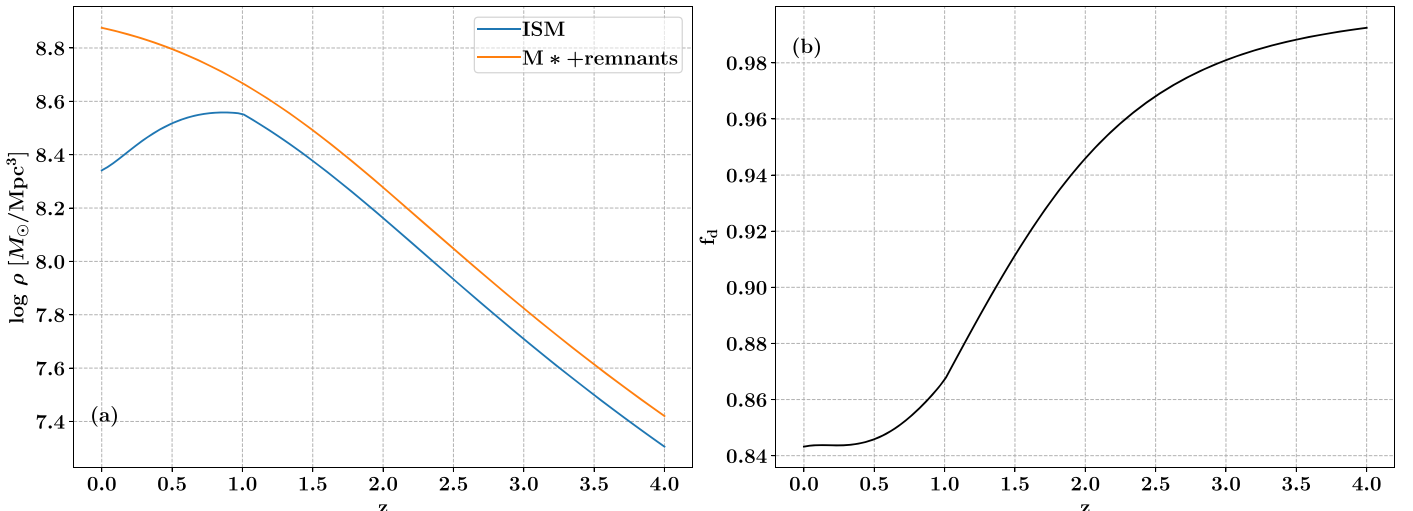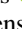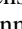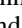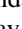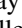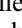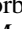

Figure A1. (a) Estimates of the stellar and ISM mass densities in galaxies vs. redshift. (b) Estimate of f_d vs. redshift.

assert that this ratio increases to unity by $z = 1$ (e.g., Tacconi et al. 2020). For our formulation of f_d, we assume that $\rho_{\rm ISM}(z)/\rho_{\rm stars}(z)$ increases as a quadratic function with time and has values 0.38 and 1 at $z = 0$ and 1 respectively, and 0.58 at the halfway time. The quantity is then taken to be unity at $z > 1$. Figure A1(a) shows plots of $\rho_{\rm stars}$ and $\rho_{\rm ISM}$ versus redshift, and Figure A1(b) presents f_d. Code that incorporates this formalism is available in the FRB repository.[13]

f_d, therefore, does not have a simple analytical expression describing it as a function of redshift. One can always approximate f_d as a polynomial expansion in z. For $z < 1$, one can obtain a reasonable approximation (relative error <5%) by truncating up to the fourth order in z:

$$f_d(z) \approx 0.843 + 0.007z - 0.046z^2 + 0.106z^3 - 0.043z^4.$$

$$(A2)$$

ORCID iDs

Sunil Simha https://orcid.org/0000-0003-3801-1496
Joseph N. Burchett https://orcid.org/0000-0002-1979-2197
J. Xavier Prochaska https://orcid.org/0000-0002-7738-6875
Jay S. Chittidi https://orcid.org/0000-0002-4985-028X
Oskar Elek https://orcid.org/0000-0003-0549-3302
Nicolas Tejos https://orcid.org/0000-0002-1883-4252
Regina Jorgenson https://orcid.org/0000-0003-2973-0472
Keith W. Bannister https://orcid.org/0000-0003-2149-0363
Shivani Bhandari https://orcid.org/0000-0003-3460-506X
Cherie K. Day https://orcid.org/0000-0002-8101-3027
Adam T. Deller https://orcid.org/0000-0001-9434-3837
Angus G. Forbes https://orcid.org/0000-0002-8700-7795
Jean-Pierre Macquart https://orcid.org/0000-0001-6763-8234
Stuart D. Ryder https://orcid.org/0000-0003-4501-8100
Ryan M. Shannon https://orcid.org/0000-0002-7285-6348

References

Barbary, K. 2016, JOSS, 1, 58
Basu, A., & Roy, S. 2013, MNRAS, 433, 1675
Behroozi, P. S., Conroy, C., & Wechsler, R. H. 2010, ApJ, 717, 379
Behroozi, P. S., Wechsler, R. H., & Wu, H.-Y. 2013, ApJ, 762, 109
Bertin, E., & Arnouts, S. 1996, A&AS, 117, 393
Bruzual, G., & Charlot, S. 2003, MNRAS, 344, 1000
Bryan, G. L., & Norman, M. L. 1998, ApJ, 495, 80
Burchett, J. N., Elek, O., Tejos, N., et al. 2020, ApJL, 891, L35
Burchett, J. N., Tripp, T. M., Prochaska, J. X., et al. 2019, ApJL, 877, L20
Calzetti, D. 2001, PASP, 113, 1449
Cen, R., & Ostriker, J. P. 1999, ApJ, 514, 1
Chabrier, G. 2003, PASP, 115, 763
Chittidi, J., Simha, S., Mannings, A., et al. 2020, arXiv:2005.13158
Cole, S., Lacey, C. G., Baugh, C. M., & Frenk, C. S. 2000, MNRAS, 319, 168
Cordes, J. M., & Lazio, T. J. W. 2003, arXiv:astro-ph/0301598
Dale, D. A., Helou, G., Magdis, G. E., et al. 2014, ApJ, 784, 83
Davé, R., Cen, R., Ostriker, J. P., et al. 2001, ApJ, 552, 473
Day, C. K., Deller, A. T., Shannon, R. M., et al. 2020, MNRAS, 497, 3335
Deng, W., & Zhang, B. 2014, ApJL, 783, L35
Elek, O., Burchett, J. N., Prochaska, J. X., & Forbes, A. G. 2020, Polyphorm, GitHub, https://github.com/CreativeCodingLab/Polyphorm
Fukugita, M. 2004, in IAU Symp. 220, Dark Matter in Galaxies, ed. S. Ryder et al. (San Francisco, CA: ASP), 227
Fukugita, M., Hogan, C. J., & Peebles, P. J. E. 1998, ApJ, 503, 518
Henley, D. B., & Shelton, R. L. 2013, ApJ, 773, 92
Hinton, S. R., Davis, T. M., Lidman, C., Glazebrook, K., & Lewis, G. F. 2016, A&C, 15, 61
Hunter, J. D. 2007, CSE, 9, 90
Inoue, S. 2004, MNRAS, 348, 999
Kauffmann, G., White, S. D., & Guiderdoni, B. 1993, MNRAS, 264, 201
Keating, L. C., & Pen, U.-L. 2020, arXiv:2001.11105
Kuntz, K. D., & Snowden, S. L. 2000, ApJ, 543, 195
Li, Y., Zhang, B., Nagamine, K., & Shi, J. 2019, ApJL, 884, L26
Lim, S. H., Mo, H. J., Lu, Y., Wang, H., & Yang, X. 2017, MNRAS, 470, 2982
Lim, S. H., Mo, H. J., Wang, H., & Yang, X. 2020, ApJ, 889, 48
Macquart, J.-P., & Koay, J. Y. 2013, ApJ, 776, 125
Macquart, J.-P., Prochaska, J. X., Shannon, R. M., et al. 2020, Natur, 581, 391
Madau, P., & Dickinson, M. 2014, ARA&A, 52, 415
McClintock, T., Rozo, E., Becker, M. R., et al. 2019, ApJ, 872, 53
McQuinn, M. 2014, ApJL, 780, L33
Morrissey, P., Matuszewski, M., Martin, D. C., et al. 2018, ApJ, 864, 93
Moster, B. P., Naab, T., & White, S. D. M. 2013, MNRAS, 428, 3121
Noll, S., Burgarella, D., Giovannoli, E., et al. 2009, A&A, 507, 1793
Oliphant, T. E. 2006, A Guide to NumPy, Vol. 1 (USA: Trelgol Publishing)
Petroff, E., Barr, E. D., Jameson, A., et al. 2016, PASA, 33, e045
Pillepich, A., Springel, V., Nelson, D., et al. 2018, MNRAS, 473, 4077
Planck Collaboration, Ade, P. A. R., Aghanim, N., et al. 2016a, A&A, 594, A13
Planck Collaboration, Aghanim, N., Arnaud, M., et al. 2016b, A&A, 594, A22
Price-Whelan, A. M., Sipőcz, B. M., Günther, H. M., et al. 2018, AJ, 156, 123
Prochaska, J. X., Macquart, J.-P., McQuinn, M., et al. 2019, Sci, 366, 231
Prochaska, J. X., & Zheng, Y. 2019, MNRAS, 485, 648
Rykoff, E. S., Rozo, E., Busha, M. T., et al. 2014, ApJ, 785, 104
Somerville, R. S., & Primack, J. R. 1999, MNRAS, 310, 1087
Springel, V., White, S. D. M., Jenkins, A., et al. 2005, Natur, 435, 629
Suresh, J., Bird, S., Vogelsberger, M., et al. 2015, MNRAS, 448, 895
Tacconi, L. J., Genzel, R., & Sternberg, A. 2020, arXiv:2003.06245
Virtanen, P., Gommers, R., Oliphant, T. E., et al. 2020, NatMe, 17, 261
White, S. D., & Frenk, C. S. 1991, ApJ, 379, 52
White, S. D. M., & Rees, M. J. 1978, MNRAS, 183, 341
Yang, X., Mo, H. J., van den Bosch, F. C., et al. 2007, ApJ, 671, 153
Yoshino, T., Mitsuda, K., Yamasaki, N. Y., et al. 2009, PASJ, 61, 805

---

[13] https://github.com/FRBs/FRB